AMLP: Adjustable Masking Lesion Patches for Self-Supervised Medical Image Segmentation

Xiangtao Wang, Ruizhi Wang, Thomas Lukasiewicz, Zhenghua Xu, *Member IEEE*

***Abstract*—Self-supervised masked image modeling (MIM) methods have shown promising performances on analyzing natural images. However, directly applying such methods to medical image segmentation tasks still cannot achieve satisfactory results. The challenges arise from the facts that (i) medical images are inherently more complex compared to natural images, and the subjects in medical images often exhibit more distinct contour features; (ii) moreover, the conventional high and fixed masking ratio in MIM is likely to mask the background, limiting the scope of learnable information. To address these problems, we propose a new self-supervised medical image segmentation framework, called Adjustable Masking Lesion Patches (AMLP), which employs Masked Patch Selection (MPS) strategy to identify patches with high probabilities of containing lesions to help model achieve precise lesion reconstruction. To improve the categorization of patches in MPS, we further introduce Relative Reconstruction Loss (RRL) to better learn hard-to-reconstruct lesion patches. Then, Category Consistency Loss (CCL) is proposed to refine patch categorization based on reconstruction difficulty, enhancing difference between lesions and backgrounds. Moreover, an Adjustable Masking Ratio (AMR) strategy is proposed to gradually increase the masking ratio over training to expand the scope of learnable mutual information. Extensive experiments on two medical segmentation datasets demonstrate the superior performances of the proposed AMLP w.r.t. the SOTA self-supervised methods; the results prove that AMLP effectively addresses the challenges of applying masked modeling to medical images and capturing accurate lesion details that are crucial for segmentation tasks.**

***Index Terms*—Self-supervised learning, masked image modeling, adjustable strategy, medical image segmentation.**

I. Introduction

SUPERVISED deep learning has achieved significant success in medical image segmentation tasks, leveraging a substantial amount of labeled data [1]–[3]. However, a vast number of medical images are generated in routine clinical practice, but annotating them requires highly specialized skills, typically performed by radiologists with extensive clinical experience. Due to the limited number of specialized radiologists, their time constraints, and the annotation efficiency, acquiring large-scale medical image datasets with precise annotations is often very hard. This limitation hinders the use of supervised learning-based segmentation methods in routine clinical practice. Consequently, recent research has seen significant efforts in self-supervised medical image segmentation [4]. Self-supervised learning aims to capture general features from unlabeled data and get the pre-trained model, and then transfer the pre-trained model into downstream tasks for fully supervised finetuning on a small amount of labeled data. Therefore, the performance of self-supervised medical image segmentation heavily relies on the quality of self-supervised pretraining.

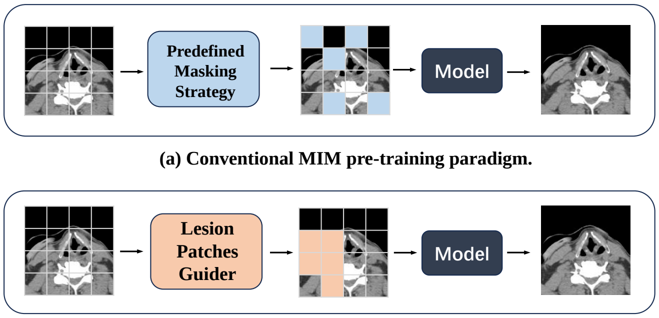

(a) Conventional MIM pre-training paradigm.

(b) Our proposed MIM pre-training paradigm.

Fig. 1: Comparison between conventional MIM pretraining paradigm and proposed AMLP. (a) Conventional approaches solve a given problem under pre-defined mask strategy. (b) Our proposed AMLP guides model to mask lesion patches to produce a challenging pretext task.

Classic self-supervised learning methods heavily rely on contrastive learning approaches. Contrastive learning (CL) aims to extract representative information by minimizing the distance between similar pairs of images while maximizing the distance between dissimilar pairs of images. However, these methods often prioritize capturing global semantics in images and may sometimes sacrifice local details and non-object regions [5]. To address these challenges, researchers, inspired by masked language modeling (MLM) in natural language processing (NLP), have turned to masked image modeling (MIM) methods to explore potential solutions. Masked image modeling is designed to reconstruct masked regions within

This work was supported by the National Natural Science Foundation of China under the grant 62276089, by the Natural Science Foundation of Tianjin, China, under the grant 24JCJQJC00200, and by the Natural Science Foundation of Hebei Province, China, under the grant F2024202064. (Corresponding author: Zhenghua Xu, e-mail: zhenghua.xu@hebut.edu.cn.)

Xiangtao Wang, Ruizhi Wang, and Zhenghua Xu are with State Key Laboratory of Reliability and Intelligence of Electrical Equipment, School of Health Sciences and Biomedical Engineering, Hebei University of Technology, Tianjin, China.

Thomas Lukasiewicz is with Department of Computer Science, University of Oxford, Oxford, United Kingdom, and the institute of Logic and Computation, Vienna University of Technology, Vienna, Austria.

images, which typically contain information about important structures.

However, applying MIM methods used in natural images directly to medical images presents limitations. This is because there are notable differences between natural and medical images, including the small size and specific morphological features of lesions, which can lead models to unintentionally overlook or fully mask critical regions, and reduce downstream performance [6], [7]. Furthermore, conventional MIM methods often employ fixed high masking ratios, which may hinder the effective capture of essential local information, emphasizing global image structures throughout encoding and decoding. This global-focused approach may result in neglecting crucial local details, e.g., the precise localization and morphology of lesions, which are indispensable in medical image analysis.

In this paper, to address these challenges, we introduce a novel self-supervised medical image segmentation method, named **A**daptive **M**asked **L**esion **P**atch (**AMLP**). Compared to existing methods, AMLP incorporates four key improvement measures: Masked Patch Selection (MPS), Relative Reconstruction Loss (RRL), Category Consistency Loss (CCL), and Adjustable Masking Ratio (AMR) strategies.

To solve the problem that conventional MIM methods are not suitable for medical images, we propose MPS. MPS can learn lesion representation by choosing the patches containing the lesion to mask. Specifically, we input all patches into k-means clustering, classify them into foreground and background, and then we rank the image patches in descending order based on the predicted probability of being foreground. Patches with higher foreground probabilities are masked first. This allows us to selectively prioritize masked image patches containing the lesion area, which can help learn lesion representation information more effectively.

However, the unsupervised k-means clustering applied in MPS may encounter the issue of potential misclassification. we further calculate the RRL for each patch, which is the ratio of the reconstruction loss to the average reconstruction loss, to ensure that the model accurately focuses on lesion patches during the training process. Additionally, we introduce the CCL, which helps the network distinguish differences between the reconstructed and original images in terms of categories, leading to a more accurate foreground-background distinction and enhancing the ability to learn lesion representation information. We also propose the AMR strategy, which gradually increases the masking ratio and the final upper limit of the masking ratio, aiding the network in learning more global information in the initial encoding phases and raising the ability of learning representation information, ultimately enhancing the acquisition of more representation information and improving overall performance.

The contributions can be summarized as follows: (i) We identify the limitations under the applications of existing self-supervised MIM learning methods in medical images, and propose a novel adjustable masking lesions patches benefits self-supervised medical image segmentation framework, named AMLP. (ii) Our AMLP framework includes four key advancements. First, we introduce MPS based on k-means clustering to improve the model's focus on lesion patches. Second, the RRL calculates relative relative reconstruction weights to emphasize challenging lesion patches. Additionally, our CCL enhances the network's ability to distinguish between reconstructed and original images, improving foreground-background separation. Furthermore, we propose AMR to further enhance the model's performance by progressively increase masking ratio during training to broaden the range of learnable mutual information. (iii) Extensive experiments were conducted on two publicly available medical segmentation datasets. The results demonstrate that our method, with only 5% or 10% labeled data, AMLP greatly outperforms the state-of-the-art self-supervised baselines. Furthermore, ablation studies confirm the effectiveness and necessity of the four improvements (i.e., MPS, RRL, CCL, AMR) for AMLP to achieve its exceptional performance.

TABLE I: Frequently Used Symbols.

Symbol	Explanation
x	original image
x_m	masked image
x_i	masked patches
$x_{\neg i}$	unmasked patches
N	number of patches
L_{pred}	reconstruction loss
L_{mean}	mean reconstruction loss of all masked patches
L_{rrl}	relative reconstruction loss
L_{ccl}	category consistency loss

II. Related Work

In recent years, self-supervised learning in computer vision has garnered attention. Early methods focused on learning feature representations through data augmentation. However, these methods tend to prioritize global semantics over local details and non-object regions [5]. A recent advancement named masked image modeling offers a fresh perspective on pretraining, which revolves around learning by reconstructing occluded image regions.

A. Contrastive learning

The objective of contrastive learning [8] aims to learn representations by drawing positive samples closer and pushing negative samples further away in the latent space, thereby distinguishing each image from others. This goal is typically achieved by applying a contrastive loss. Currently, many contrastive learning methods have found successful applications in medical image segmentation. For instance, SimCLR [9] employs a contrastive loss function and multi-layer feature representation learning to facilitate self-learning on large-scale unlabeled data, thereby enhancing the model's representational and generalization capabilities, but this method relies too much on data augmentation. To mitigate this issue, MoCo [10] further bolsters the model's robustness and discriminative performance by introducing momentum contrastive learning and a nonlinear contrastive loss function, expanding the set of negative samples and enhancing sample variability, but it only focuses on sample-level information and ignores details.

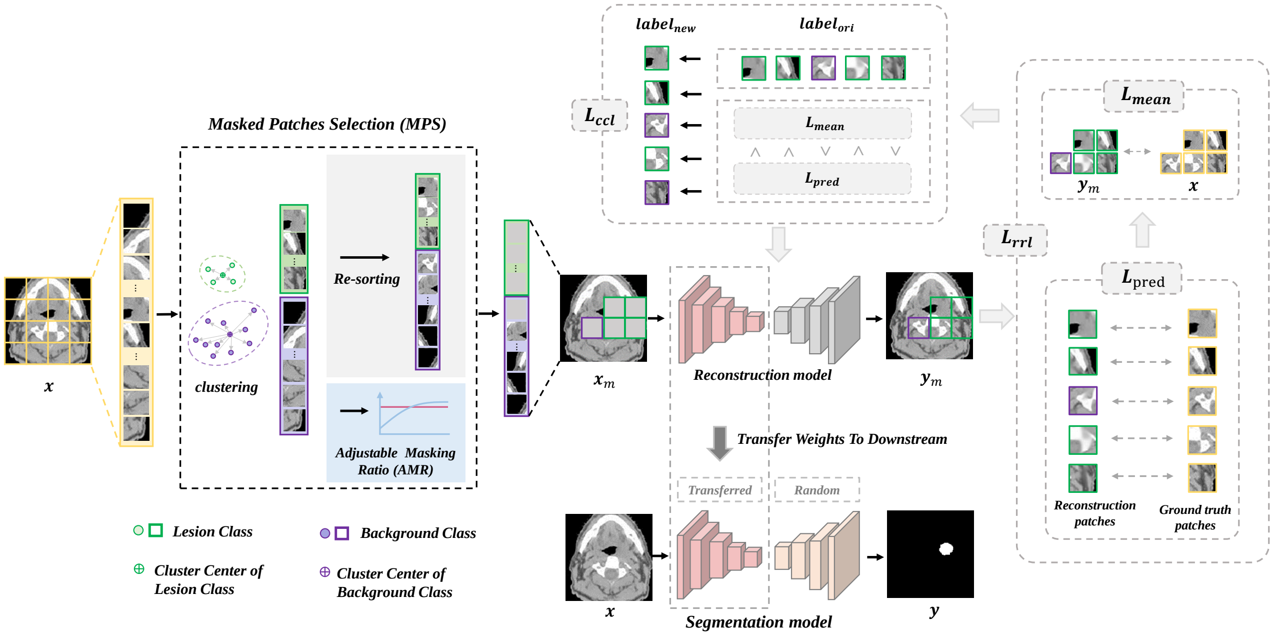

Fig. 2: Illustration of our proposed AMLP architecture. The image x is divided into N patches, which serve as the input of K-means clustering. The clustering process classifies the patches into two categories: lesion and background categories, and selectively mask them by the order of lesion-background. Then, the masked image is input into the reconstruction network for reconstruction. After pretraining, only the encoder of reconstruction network is transferred to downstream segmentation model.

Considering that possible negative pair construction errors could affect model performance, BYOL [11] promotes the learning of more discriminative feature representations through bootstrapping methods and multi-task training, achieving significant improvements in SSL performance. To further process fine-grained features and complex scenes, SwAV [12] proposes a method for unsupervised learning of visual features by contrastive cluster assignment, achieving effective feature and representation learning by comparing the similarity of samples in different cluster groupings. However, more professional solutions are needed in the field of medical image analysis, G-L [13] proposes to combine a local contrastive strategy (i.e., using 3D inter-layer location information for contrastive learning) with a global contrastive strategy to learn beneficial information representations. To achieve deeper feature learning, PCRL [14] introduces Preservational Contrastive Representation Learning to reconstruct diverse contexts using representations learned from the contrastive loss. To capture rich semantic information at both global and local levels, vox2vec [15] models voxel representations through a Feature Pyramid Network (FPN), producing similar representations for the same voxels and unique representations for different voxels in various augmentation contexts, thereby learning multi-scale representations that capture global semantics and local semantics. While these multi-scale representations are effective, they may not guarantee optimal alignment between features from different semantic levels. SAL [16] introduces a self-supervised alignment learning framework that enhances consistency in feature learning by aligning pixel-level features of matched structures across different semantic levels, thereby improving the robustness of medical image segmentation. Besides the methods rely on invariance under certain intensity-based augmentations and geometric augmentations, Pix2Rep [17] proposes a pixel-level representation learning framework based on equivariance under geometric transformations. By explicitly modeling how pixel-level features should transform under different geometric operations, Pix2Rep enables more precise and geometrically-aware feature learning.

However, these methods often prioritize global semantic features over image details and non-subject regions [5], affecting the performance in downstream segmentation tasks.

B. Masked image modeling

Masked image reconstruction involves masking specific image blocks and using a reconstruction network to recover them. For instance, MAE [18] utilizes an asymmetric encoder-decoder structure, dividing the image into equal-sized blocks and predicting the masked block based on the unmasked block of the image. At the same time, SimMIM [19] adjusts decoder weights and incorporates visible and masked patches as input, achieving results comparable to MAE. To address the imbalance problem of feature learning in different regions of the image, Maskfeat [20] introduces the Masked Feature Prediction method, enabling the model to predict masked features by randomly covering patches in the HOG feature map. ConvMAE [21] enhances semantic information acquisition through MAE-based multi-scale encoding operations to learn more refined and discriminative feature representations. To further expand the application scope of masked image modeling, BEiT V2 [22] incorporates a discrete visual codebook generated by vector-quantized knowledge distillation (VQ-KD) and introduces a pre-training stage for high-level semantic abstraction. Despite these advancements, model learning efficiency remains low. BootMAE [23] introduces a supervised Bootstrapped Masked Autoencoder, using masked autoencoding objectives for patch-level feature prediction tasks and an additional supervised bootstrapping signal. To optimize for the specificity of medical imaging, SelfMedMAE [24] proposes a self-pretraining paradigm with MAE for medical image analysis tasks, pretraining a ViT on the target data's training set instead of another dataset.

These methods solve specific problems under predefined masking strategies [25], [26]. Unlike existing methods, AMLP considers the unique importance of lesion areas in medical images, learns key representation information by specifically masking lesion areas, and achieves gradual feature learning through an adjustable masking ratio adjustment strategy. This allows AMLP to learn representations that are more beneficial to downstream segmentation tasks and achieve more accurate lesion segmentation.

III. Methodology

Fig. 2 provides an overview of our proposed AMLP, which comprises four key components: Masked Patches Selection(MPS), Relative Reconstruction Loss (RRL), Category Consistency Loss (CCL), and Adjustable Masking Ratio (AMR). Specially, we commence by elucidating the masked patches selection strategy in Sec. III-A. Furthermore, Sec. III-B details the relative reconstruction loss, while Sec. III-C introduces the category consistency loss. Subsequently, the adjustable masking strategy is presented in Sec. III-D.

A. Masked Patches Selection

Given that most current efforts in masked image modeling concentrate on natural images, with scant applications in medical images, we propose a masked patches selection strategy tailored specifically for medical images.

Overall, the proposed masked patches selection (MPS) strategy is implemented by filtering and masking image patches containing lesions. First, the k-means algorithm is used for preliminary classification of the image patches, which are then prioritized based on their probability of containing lesions. Finally, the MPS selects and masks patches with higher probabilities to help the model specifically learn lesion features.

Before clustering begins, the input medical image x is divided into N equal-sized patches. Each patch is independently vectorized into a one-dimensional vector. Subsequently, the vectorized results of all image patches are concatenated into a two-dimensional array for clustering using k-means.

Since our ultimate goal is lesion segmentation, the k-means algorithm only needs to classify all image patches into two categories: foreground (i.e., patches containing lesion areas) and background (i.e., patches not containing lesions). Specifically, the k-means algorithm first randomly selects two patches as initial cluster centers. For each patch, calculate its distance to the two cluster centers and assign it to the category corresponding to the nearest one. Then, for each category, recalculate its cluster center (i.e., the centroid of all samples belonging to that category). These processes iterate continuously to optimize the clustering results.

We divide all patches into two categories $x = \{x_i, x_{\neg i}\}$ through k-means clustering. Considering the lesion areas are smaller than background areas, we set the group with the lesser number is the foreground x_i and the bigger number is the background $x_{\neg i}$. They are assigned category labels of 1 and 0 respectively, e.g., $label_{x_i} = 1$, $label_{x_{\neg i}} = 0$. Then, according to the probability of being judged as the foreground, they are sorted from large to small, and a foreground-background ordered mask is performed according to the mask ratio. Specially, the larger the distance from each patch to the center point of the foreground category, the greater the dissimilarity between its feature and the foreground cluster center, and accordingly, the greater the possibility that the patch is classified as foreground [27].

B. Relative Reconstruction Loss

In the Masked Patch Selection (MPS), the sole reliance on unsupervised k-means clustering may lead to potential misclassification issues. Therefore, it is imperative to assist the network in accurately identifying foreground image patches. The most common method for determining whether a patch is foreground region is comparing the reconstruction loss L_{pred} of a single patch, such as the L_2 loss used in MAE. (In this paper, we denote the L_2 loss as L_{pred}.) A higher loss value indicates a greater difficulty in reconstruction, which means it is more likely to be a foreground region. However, as training progresses, the scale of the L_{pred} loss diminishes. When the loss values become very small, the model struggles to effectively differentiate the reconstruction difficulty of different patches, making it challenging to identify which patches need focused attention and masking. Therefore, the exclusive use of one patch's reconstruction loss is not the optimal choice.

To enhance the model's focus on the foreground regions more precisely, we propose a relative loss based on the Relative Reconstruction Loss (RRL). Unlike comparing the reconstruction loss of a single patch, the RRL dynamically evaluates the importance of each patch by calculating the ratio of a patch's reconstruction loss to the average reconstruction loss of all masked patches. When a patch's reconstruction loss is higher than the average, it indicates that the patch is more challenging in the reconstruction task, which usually means it is a foreground region. Consequently, RRL encourages the model to pay special attention to these regions, as they are more likely to contain important lesion information. Through this method, the model can more effectively identify and concentrate on foreground regions that require significant masking, thereby alleviating the issue of misclassification.

Specifically, we compute the relative reconstruction loss L_{rrl} by calculating the ratio of reconstruction loss L_{pred} for an patch to the average reconstruction loss of all masked image patches L_{mean}. The formula of L_{rrl} is as follows:

$$L^i_{rrl} = L^i_{pred}/L_{mean}, \tag{1}$$

where L^i_{pred} indicates the L_{pred} loss of $i-th$ patch. And the formula of L_{mean} is below:

$$L_{mean} = \sum_{i=1}^{N}(L^i_{pred})/N. \tag{2}$$

where N indicates the number of masked patches, and L^i_{pred} indicates the L_{pred} loss of $i-th$ patch.

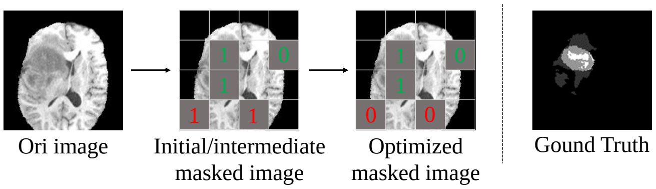

Fig. 3: Visualization of the patch category correction process during training, where 1 represents the lesion category, and 0 represents the background category, and green represents correctly classified image patches, and red represents incorrectly classified image patches.

C. Category Consistency Loss

Furthermore, we propose the Category Consistency Loss (CCL) to enhance the network's ability to distinguish between foreground and background to further address the issue of misclassification. The CCL emphasizes patches whose classifications change during training by measuring the consistency between $Label_{new}$ and $Label_{ori}$.

Specifically, regarding the k-means clustering results, each patch is assigned a category label $Label_{ori}$ after k-means clustering, where the foreground category is represented by 1 ($Label_{ori} = 1$) and the background category is represented by 0 ($Label_{ori} = 0$). Concerning the relative values of L_{pred} and L_{mean}, if $L_{pred} \geq L_{mean}$, the patch is considered more important compared to the average patch, and it is more likely to belong to the lesion category; if $L_{pred} < L_{mean}$, it is more likely to belong to the background category.

CCL updates the category labels of the patch clustering results according to the following rules: (i)If the k-means clustering result for a patch is consistent with the relative values of L_{pred} and L_{mean} (i.e., $Label_{ori} = 1$ and $L_{pred} \geq L_{mean}$, or $Label_{ori} = 0$ and $L_{pred} < L_{mean}$), the new category label for the patch remains unchanged; (ii)If the k-means clustering result for a patch is inconsistent with the relative values of L_{pred} and L_{mean} (i.e., $Label_{ori} = 1$ and $L_{pred} < L_{mean}$, or $Label_{ori} = 0$ and $L_{pred} \geq L_{mean}$), the new category label for the patch is randomly chosen from [0,1]. The reason for adopting the second update strategy is that it is difficult to determine which is more accurate between the k-means clustering result and the relative values of L_{pred} and L_{mean}. Therefore, to balance these two situations, we use a random selection method.

To facilitate a more intuitive understanding of this process, we have visualized the patch category correction during training in Figure 3. Correct and incorrect classifications (compared to the ground truth) are highlighted in green and red, respectively. As training progresses, the two misclassified foreground red image patches (label 1) are corrected to background (label 0), indicating that our proposed AMLP can dynamically adjust and improve the classification results of image patches during the model learning process.

When $label_{new} \neq label_{ori}$, indicating a change in patch categorization during training, we calculate CCL using the following formula:

$$\begin{aligned} L_{ccl} = &-[label_{new} \times \log(label_{ori} + \xi) \\ &+(1 - label_{new}) \times \log(1 - label_{ori} + \xi)]. \end{aligned} \tag{3}$$

where $Label_{ori}$ and $Label_{new}$ can only take the values 0 and 1, and $\xi = 1e - 1$ is used to prevent $\log(0)$. After each training epoch, the $label_{new}$ will replace the current $label_{ori}$ for the corresponding patch to enable dynamic label updating. Furthermore, we observed that the final results converge to the first update rule.

The overall loss of AMLP is defined as:

$$L_{all} = L_{pred} + L_{rrl} + L_{ccl}. \tag{4}$$

D. Adjustable Masking Ratio

Given that a higher mask ratio can force the model to learn more challenging and rich features. We question whether the commonly used fixed masking ratio of 75% in studies like MAE [18] and SimMIM [19] is the upper limit. Could we further improve the representation learning ability and achieve better performance by increasing the upper limit of the masking ratio?

To overcome this limitation, we propose an innovative dynamic masking ratio strategy, where the masking ratio gradually increases from an initial value as training progresses. The initial masking ratio σ_0 is set to 25%, based on experimental findings in MAE [18]. Furthermore, as training progresses, the masking ratio increases according to the following equation and finally reaches 80%:

$$\sigma = \sigma_0 + \ln(x_e)/\tau, \tag{5}$$

where x_e denotes the training epoch, and τ is a manually defined constant.

By integrating the masked patches selection strategy with adjustable masking ratio strategy, we can compute the number of masked patches n_m and the masked image x_m, where $n_m = \lfloor N \times \sigma \rfloor$. Then, the masked image x_m is input into the reconstruction network to reconstruct the masked patches.

It is worth noting that AMLP uses the k-means clustering algorithm to select masked patches, introducing a certain degree of randomness. Although we later incorporate RRL and CCL to mitigate the inherent misclassification issues of k-means clustering, the lower masking rate in the early stages of training, combined with the randomness of the k-means algorithm in selecting lesion patches, ensures that the model can learn discriminative features from unmasked lesion patches. Therefore, even under a high masking ratio later on, where lesions are completely masked, the model can still perform lesion recognition and segmentation tasks based on its learned high representational capacity.

IV. Experiments and Results

Datasets: To validate the effectiveness of our proposed AMLP, we conduct extensive evaluations on two publicly available medical image datasets, Hecktor [28] and BraTS2018 [29]. (i) *Hecktor.* The dataset comes from the MICCAI 2020 challenge called HEad and the neCK TumOR Segmentation Challenge (Hecktor) for Head and Neck Tumor Segmentation. It contains 201 3D head and neck PET-CT scans. (ii) *BraTS2018.* This dataset was released by the BraTS'18 challenge hosted by MICCAI 2018 for brain tumor segmentation, including three hierarchical labels: WT (whole tumor), ET (enhancing tumor), and TC (tumor core). It contains four modalities: T1, T1CE, T2 and FLAIR.

TABLE II: The DSC and Sen results of AMLP and the state-of-the-art fully-supervised and self-supervised segmentation methods on the Hecktor and BraTS2018 datasets with 5%, and 10% labeled data in terms of DSC and Sen.

	Methods	**Hecktor**				**BraTS2018**							
	Modality	CT		PET		T1CE		T2		FLAIR		T1	
	Metrics	DSC↑	Sen↑	DSC↑	Sen↑	DSC↑	Sen↑	DSC↑	Sen↑	DSC↑	Sen↑	DSC↑	Sen↑
5%	Sup	0.1740	0.2337	0.5452	0.7044	0.3234	0.2703	0.3952	0.4371	0.4035	0.4837	0.1743	0.2702
	SimCLR [9]	0.1733	0.2527	0.5720	0.7143	0.5403	0.5737	0.4310	0.5870	0.4342	0.5396	0.2908	0.4376
	BYOL [11]	0.1967	0.2555	0.4487	0.5603	0.5245	0.4321	0.4377	0.5590	0.4561	0.6297	0.2811	0.4545
	SwAV [12]	0.2307	0.2483	0.5517	0.7091	0.5252	0.4321	0.4160	0.5564	0.4346	0.6052	0.2277	0.4466
	G-L [13]	0.1754	0.1719	0.5615	0.6993	0.3195	0.4130	0.4412	0.5281	0.4355	0.5603	0.2137	0.2917
	PCRL [14]	0.2374	0.2777	0.5605	0.7130	0.5158	0.4572	0.4251	0.5227	0.4453	0.6124	0.2695	0.4365
	MAE [18]	0.2560	0.2966	0.5931	0.7301	0.5465	0.5276	0.4395	0.5134	0.4368	0.6108	0.2734	0.4596
	MaskFeat [20]	0.2561	0.2894	0.5900	0.7277	0.5332	0.5173	0.4492	0.5012	0.4442	0.5937	0.2834	0.4542
	SimMIM [19]	0.2413	0.2972	0.5892	0.7239	0.5421	0.5012	0.4289	0.4901	0.4525	0.6013	0.2801	0.4297
	ConvMAE [21]	0.2611	0.3042	0.6042	0.7431	0.5552	0.5414	0.4497	0.5338	0.4247	0.6243	0.2979	0.4865
	BEiT V2 [22]	0.2759	0.3153	0.6133	0.7548	0.5508	**0.5779**	0.4504	0.5587	0.4501	**0.6299**	0.3027	0.4891
	BootMAE [23]	0.2593	0.2978	0.5988	0.7345	0.5431	0.5358	0.4496	0.5134	0.4412	0.6164	0.2908	0.4739
	SelfMedMAE [24]	0.2699	0.3115	0.6235	0.7439	0.5523	0.5516	0.4557	0.5284	0.4594	0.6104	0.2944	0.4751
	vox2vec [15]	0.2791	0.3193	0.6240	0.7541	0.5632	0.5635	0.4605	**0.5621**	0.4623	0.6229	0.3011	0.4801
	Ours	**0.2905**	**0.3347**	**0.6296**	**0.7665**	**0.5762**	0.5482	**0.4721**	0.5023	**0.4693**	0.6136	**0.3297**	**0.5023**
10%	Sup	0.2541	0.2703	0.5769	0.7067	0.4451	0.3696	0.4288	0.4716	0.4489	0.6225	0.2476	0.3366
	SimCLR [9]	0.2951	0.3895	0.5779	0.7145	0.6024	0.6217	0.4846	0.5729	0.4720	0.5217	0.3551	0.4868
	BYOL [11]	0.3088	0.3930	0.5891	0.6990	0.5991	0.6323	0.4850	0.5710	0.4763	0.6329	0.3458	0.3535
	SwAV [12]	0.2690	0.3340	0.5771	0.7004	0.5515	0.5646	0.4587	0.5794	0.4543	0.6084	0.2914	0.4694
	G-L [13]	0.2784	0.2945	0.5923	0.7304	0.4575	0.5045	0.4645	0.5718	0.4504	**0.6691**	0.2685	0.4086
	PCRL [14]	0.2907	0.3985	0.5904	0.7039	0.5649	0.5713	0.4726	0.5672	0.4601	0.6453	0.3083	0.4461
	MAE [18]	0.3195	0.4143	0.6058	0.7155	0.5881	0.5947	0.4765	0.5256	0.4587	0.6178	0.3578	0.4878
	MaskFeat [20]	0.3078	0.4077	0.5955	0.7132	0.6065	0.5864	0.4613	0.5103	0.4625	0.6154	0.3351	0.4800
	SimMIM [19]	0.2920	0.4025	0.5872	0.7221	0.5932	0.5701	0.4592	0.5082	0.4572	0.5921	0.3246	0.4725
	ConvMAE [21]	0.3369	0.4273	0.6099	0.7183	0.6106	0.6208	0.5031	0.5667	0.4915	0.6246	0.3617	0.5123
	BEIT V2 [22]	0.3470	0.4388	0.6293	0.7217	0.6139	0.6315	0.5079	0.5897	0.4862	0.6446	0.3690	0.5334
	BootMAE [23]	0.3225	0.4243	0.6221	0.7155	0.6203	0.6032	0.4857	0.5321	0.4751	0.6093	0.3624	0.5011
	SelfMedMAE [24]	0.3403	0.4313	0.6121	0.7204	0.6177	0.6159	0.5019	0.5330	0.4825	0.6264	0.3740	0.5322
	vox2vec [15]	0.3509	0.4420	0.6285	0.7213	0.6268	**0.6379**	0.5107	**0.5975**	0.4904	0.6313	0.3798	0.5461
	Ours	**0.3690**	**0.5004**	**0.6314**	**0.7331**	**0.6343**	0.6023	**0.5194**	0.5482	**0.4971**	0.6324	**0.3815**	**0.5782**
	Sup (50%)	0.3440	0.4331	0.6252	0.6582	0.5941	0.5324	0.5094	0.5328	0.4830	0.5664	0.3581	0.4564
	Sup (100%)	0.3927	0.4736	0.6475	0.7307	0.7453	0.7204	0.5556	0.5575	0.5164	0.6561	0.4207	0.4923

Baselines: We consider two primary categories of baselines: fully supervised and self-supervised learning. For fully supervised learning, we use a randomly initialized U-Net architecture without self-supervised pretraining. We train this model from scratch with annotations at 5%, 10%, 50%, and 100% granularity levels to comprehensively assess the impact of self-supervised pretraining. As for self-supervised learning, we have two subcategories: contrastive learning and masked image modeling. In contrastive learning, we use SimCLR [9], BYOL [11], SwAV [12], G-L [13], PCRL [14], and vox2vec [15] as baselines for their effectiveness in capturing informative representations. For masked image modeling, we consider state-of-the-art methods such as MAE [18], Maskfeat [20], SimMIM [19], ConvMAE [21], BEiT V2 [22], BootMAE [23], and SelfMedMAE [24] which are known for modeling complex relationships in medical images through mask-based objectives. We evaluate the quality of learned representations by transferring them to downstream segmentation tasks, performing end-to-end fine-tuning. This structured approach to baselines ensures a systematic evaluation of AMLP in comparison to a diverse set of benchmarks.

Pre-processing: We apply the following pre-processing steps: (i) re-sampling of all volumes and corresponding labels to a fixed pixel size $1.0 \times 1.0 \times 1.0\ mm^3$ using nearest-neighbour interpolation, intensity normalization of each 3D volume, clip the value to the $[1, 99]$ percentiles to remove extreme pixel values (such as too high or too low values), avoiding these extreme values from having a negative impact on subsequent processing and model training and normalize the image with mean and std for region nonzero to help the model learn image features more effectively. Therefore, reduce outliers in pixel values and enhance the contrast of the image, making model training more efficient.

(ii) all 2D images and corresponding 2D labels are obtained from the z-axis of 3D volumes. The dimension d for each dataset are: (a) Hecktor: d = 144×144, and (b) BraTS2018: d = 160×160.

Implementation details: Our AMLP is implemented based on Torch 1.6.0 and CUDA-10.1. All experiments are done on 8 GeForce RTX 2080 GPUs. For self-supervised learning, the AdamW [30] optimizer is used, with a learning rate of $1e-4$. The temperature parameter t is set to 0.1. The batch size is 48 for Hecktor and 36 for BraTS2018. And a total of 800 epochs is trained. The patch size of the Hecktor dataset and BraTS2018 dataset images is 16×16, and the corresponding numbers of the image patches are 81 and 100 respectively. Besides, single-modality data is used for BraTS (T1CE, T2, Flair, and T1) and Hecktor (CT, and PET) datasets. For transfer learning, the U-Net [31] for downstream segmentation task is also trained with AdamW optimizer. The initial learning rate is $1e-4$, the weight decay is 0.0001, and the learning rate strategy is cosine decay. When using 5% labels, batch size is set to 31 for Hecktor and 56 for BraTS2018. For 10% labels, batch size is set to 90 for Hecktor and 70 for BraTS2018. To make network convergence, 70 epochs are trained for Hecktor and BraTS2018.

TABLE III: The BIoU and HD95 results of AMLP and the state-of-the-art fully-supervised and self-supervised segmentation methods on the Hecktor and BraTS2018 datasets with 5%, and 10% labeled data in terms of BIoU and HD95.

	Methods	**Hecktor**				**BraTs2018**							
	Modality	CT		PET		T1CE		T2		FLAIR		T1	
	Metrics	BIoU↑	HD95↓	BIoU↑	HD95↓	BIoU↑	HD95↓	BIoU↑	HD95↓	BIoU↑	HD95↓	BIoU↑	HD95↓
5%	Sup	0.0690	62.7115	0.2493	69.0963	0.1487	55.0727	0.1330	47.4584	0.2055	33.2086	0.0484	59.5963
	SimCLR [9]	0.0718	61.0090	0.2627	64.9785	0.1492	54.0091	0.1357	46.3305	0.2072	32.7433	0.0567	57.6039
	BYOL [11]	0.0845	60.8153	0.2793	60.2143	0.1504	49.3725	0.1501	44.2871	0.2103	31.0754	0.0609	54.4291
	SwAV [12]	0.0711	61.9957	0.2678	61.8257	0.1495	52.2436	0.1401	45.8792	0.2083	31.5867	0.0589	56.4368
	G-L [13]	0.0703	62.2405	0.2561	62.0235	0.1506	52.0623	0.1463	45.9033	0.2100	32.0056	0.0628	57.2391
	PCRL [14]	0.0904	60.1120	0.2743	62.6295	0.1562	53.2362	0.1533	46.0758	0.2154	31.9603	0.0701	58.0055
	MAE [18]	0.0999	58.7935	0.2802	54.9321	0.1472	48.2318	0.1489	43.1123	0.2106	30.2385	0.0842	53.5203
	MaskFeat [20]	0.1067	59.0087	0.2799	58.9967	0.1505	49.0699	0.1463	43.7748	0.2117	32.7451	0.0775	54.2226
	SimMIM [19]	0.0793	60.6234	0.2743	58.4102	0.1461	51.0855	0.1382	44.2219	0.2095	31.1998	0.0589	55.0105
	ConvMAE [21]	0.1053	58.5928	0.2955	50.6654	0.1593	46.8451	0.1574	41.0145	0.2140	29.1014	0.1063	51.1002
	BEiT V2 [22]	0.1374	57.4124	0.2994	48.2849	0.1607	46.3542	0.1623	f40.3721	0.2152	28.5621	0.1112	50.2631
	BootMAE [23]	0.1201	59.5928	0.2836	52.7976	0.1512	47.1273	0.1537	41.2457	0.2128	29.8902	0.0928	52.4317
	SelfMedMAE [24]	0.1414	59.7325	0.2910	51.1758	0.1672	46.1121	0.1608	40.1080	0.2104	29.7491	0.1074	51.4210
	vox2vec [15]	0.1455	58.3407	0.3017	47.3999	0.1692	45.8761	0.1638	**40.0012**	0.2139	28.9602	0.1130	50.4658
	Ours	**0.1514**	**57.2823**	**0.3113**	**40.5376**	**0.1723**	**44.2326**	**0.1750**	40.6362	**0.2156**	**28.2352**	**0.1157**	**50.2342**
10%	Sup	0.1224	64.0604	0.3199	41.8627	0.1643	50.9107	0.1510	43.9483	0.1724	30.4918	0.1042	52.8203
	SimCLR [9]	0.1504	46.3870	0.3581	66.4539	0.2758	37.6094	0.2020	38.0898	0.2203	28.5869	0.1247	46.2637
	BYOL [11]	0.1501	58.9947	0.3397	55.0181	0.2901	36.1710	0.1820	42.4852	0.2075	27.9066	0.1201	39.8026
	SwAV [12]	0.1543	59.5009	0.3573	50.8417	0.2287	46.0846	0.1889	44.0658	0.2036	38.6023	0.1035	61.8490
	G-L [13]	0.1462	57.9235	0.3473	53.8722	0.2490	48.6177	0.1803	41.9554	0.2048	36.1221	0.0969	53.0828
	PCRL [14]	0.1593	57.1364	0.3603	50.1351	0.2587	40.8316	0.1974	41.0274	0.2109	35.1126	0.1197	50.1286
	MAE [18]	0.1702	55.2376	0.3445	46.1427	0.3113	32.7709	0.2167	32.9846	0.2145	26.9349	0.1182	35.9123
	MaskFeat [20]	0.1634	57.2447	0.3618	47.6183	0.3024	33.2451	0.1987	35.6779	0.2109	27.3426	0.1245	37.5428
	SimMIM [19]	0.1601	58.3412	0.3511	48.8915	0.2975	34.8762	0.2063	37.5124	0.2096	29.8875	0.1223	39.3501
	ConvMAE [21]	0.1882	50.3523	0.3739	41.7655	0.3421	25.9865	0.2301	28.0147	0.2012	25.6731	0.1356	27.8754
	BEIT V2 [22]	0.1990	48.7192	0.3899	39.8887	0.3578	22.4567	0.2253	23.8829	0.2218	24.2587	0.1428	24.7159
	BootMAE [23]	0.1788	54.5214	0.3612	42.9639	0.3182	27.9943	0.2173	30.5402	0.2186	25.9823	0.1324	33.7837
	SelfMedMAE [24]	0.1960	46.6575	0.3933	40.1080	0.3535	23.6667	0.2105	26.2442	0.2182	25.1368	0.1397	27.1394
	vox2vec [15]	0.2098	45.7324	0.3959	38.0991	0.3609	21.0440	**0.2304**	25.9604	0.2247	**23.9486**	**0.1443**	25.5126
	Ours	**0.2368**	**44.2361**	**0.4032**	**35.3453**	**0.3745**	**20.3453**	0.2253	**23.2375**	**0.2234**	25.1484	0.1402	**23.5632**
	Sup (50%)	0.1882	46.3327	0.3713	36.0685	0.3557	23.8802	0.2030	23.6540	0.2354	24.7391	0.1358	22.6528
	Sup (100%)	0.2398	50.0361	0.3928	34.7032	0.3962	18.8440	0.2238	19.7038	0.2477	22.0652	0.1582	20.8641

During implementation, the AMR masking rate starts at 25% and is gradually increased to 80% during training. For datasets with extremely subtle lesions, performance can be improved by reducing the initial masking rate and increasing τ. Meanwhile, the MPS strategy assumes that smaller clusters correspond to lesion classes. In atypical cases where lesions occupy most of the image, larger clusters can be assigned to lesion classes.

Besides, all baselines are implemented and run using similar procedures and settings as those in their original papers, where all self-supervised methods are learned in a two-stage learning way, i.e., first pre-trained using only unlabeled data and then fine-tuned using limited labeled data.

Network Architecture: We use the U-Net, which includes four downsampling and upsampling modules, as a segmentation backbone network for all methods. Each downsampling module consists of two 3×3 convolutions and a 2×2 maxpooling with stride 2, while each upsampling module consists of two 3×3 convolutions and a 2×2 transposed convolution with stride 2. This U-Net network also serves as the backbone network of AMLP.

Fine-tuning:

In the upstream pre-training task, our model reconstructs masked images. During this stage, the reconstructed images serve only to optimize the network, compelling it to learn more discriminative lesion information and develop robust feature representations for downstream tasks. Subsequently, we transfer the weights of the pre-trained encoder to the downstream model, while its decoder is randomly initialized. For the downstream segmentation task, the model does not use any generated images as input; instead, it performs lesion segmentation directly on real medical images during both the fine-tuning and inference phases.

Evaluation metrics: We use four key metrics to evaluate our methods: Dice Similarity Coefficient (DSC) [32], Sensitivity (Sen), Mean Intersection of Union Boundaries (BIoU) [33], and 95% Hausdorff Distance (HD95). DSC and Sen reflect similarity metrics, while BIoU and HD95 measure distance-related aspects.

Specific formulas for these metrics are as follows:

$$DSC = \frac{2 \times TP + \epsilon}{T + P + \epsilon}, \tag{6}$$

$$SEN = \frac{TP + \epsilon}{TP + FN + \epsilon}, \tag{7}$$

$$BIoU = \frac{(G_d \cap G) \cap (P_d \cap P)}{(G_d \cap G) \cup (P_d \cap P)}, \tag{8}$$

$$HD95 = max_{k95\%}[d(P, G), d(G, P)], \tag{9}$$

where TP, FP, and FN are true positive, false positive, and false negative, respectively. P is the prediction binary mask, G is the ground truth binary mask, P_d and G_d are the sets of pixels in the boundary region of the binary mask.

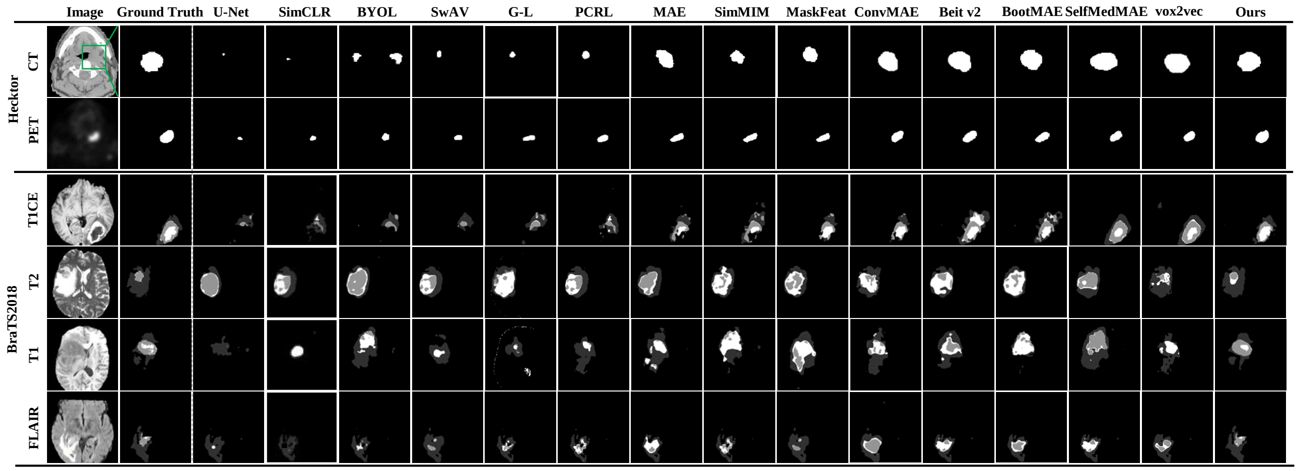

Fig. 4: Visualized segmentation results on the Hecktor and BraTS2018 datasets with 10% labeled data. The first two rows are the results of the Hecktor dataset, specifically the slice number are CHUM044_slice_098 (PET) and CHUM012_slice_089 (CT), where the head and neck tumor (only one type of tumor) is marked with white in the segmentation results. The last four rows are the results of the BraTS2018 dataset, specifically the slice number are Brats18_TCIA02_608_1_059 (T1CE), Brats18_CBICA_AQO_1_084 (T2), Brats18_CBICA_AUN_1_081 (T1), and Brats18_2013_18_1_067 (FLAIR), where WT (whole tumor), ET (enhancing tumor), and TC (tumor core) are marked with light gray, medium gray and white, respectively. As observed, our segmentation results are closer to ground truth and better than other methods.

A. Main Results

To investigate the effectiveness of our proposed AMLP, we conduct experiments on two datasets and compare its performance with two kinds of state-of-the-art baselines: Fully Supervised Baseline (i.e., Fully Supervised) and Self-Supervised Baselines (i.e., SimCLR, BYOL, SwAV, MAE, Maskfeat, SimMIM, ConvMAE, BEiT v2, BootMAE). For a fair comparison, we use the same backbone network (U-Net) with 5% and 10% annotations across all methods. The experimental results are shown in Table II and Table III, which respectively refer to two types of indicators: similarity metrics (i.e., DSC and Sen) and distance metrics (i.e., BIoU and HD95). For ease of comparison, we report only the average results for different modalities of the BraTS2018 dataset in the main experimental results. This average is obtained by calculating the individual segmentation results for the three different hierarchical labels and then averaging them. The visualization of the segmentation results of AMLP and other methods are shown in Fig. 4.

As shown in Table II and Table III, AMLP generally outperforms all the state-of-the-art self-supervised medical image segmentation baselines in terms of all evaluation metrics and two small label-ratio settings (i.e., 5% and 10%) on both datasets, and its performances are similar to (and sometimes even better than) the fully supervised solution using much higher ratios (i.e., 50% and 100%) of label data. This observation proves that the proposed AMLP can achieve superior medical image segmentation performances using only a small number of annotations, which thus greatly reduces the labeling workload of applying intelligent medical image segmentation systems in clinical practices. Detailed analysis is as follows.

Comparison with state-of-the-art fully-supervised methods. As shown in Table II and Table III, self-supervised learning methods (including the proposed AMLP) achieve much better segmentation performances than the fully supervised baseline with the same ratio of labeled data. This enhancement stems from the ability of self-supervised methods to extract valuable insights from the unlabeled data.

Furthermore, AMLP generally outperforms the baseline model that is fully supervised learning from scratch by a large margin with 5% and 10% annotations. The performance of AMLP with 5% annotations can be close to or even better than that of the fully supervised method with 50% annotations. As for 10% annotations, AMLP not only outperforms the fully supervised method with 50% annotations but also outperforms the fully supervised method with 100% annotations in the PET modality on Hecktor. Specifically, in the case of 5% annotation on the CT modality of the Hecktor dataset, we observe that AMLP outperforms the fully supervised method by 11.65% for DSC, 10.1% for Sen, and 8.24% for BIoU, and 4.4292 for HD95; while on the T1 modality of the BraTS2018 dataset, AMLP outperforms the fully supervised method by 15.54% for DSC, 23.21% for Sen, and 6.73% for BIoU, and 9.3621 for HD95. This is because the ability of our method to learn more valuable representations from a large amount of unlabeled data, thereby improving the performance of downstream segmentation models.

Comparison with state-of-the-art self-supervised methods. In Table II and Table III, we compared AMLP with state-of-the-art self-supervised methods. AMLP consistently outperforms these methods across nearly all cases on both datasets, which demonstrates AMLP's ability to extract more comprehensive information and features from unlabeled multimodal data compared to current self-supervised contrastive learning baselines, resulting in superior medical image segmentation. For example, in the case of 5% annotation on CT modality of the Hecktor dataset, we observe that AMLP outperforms the fully supervised method by 1.46% for DSC, 1.94% for Sen, and 1.4% for BIoU; while on T1 modality of the BraTS2018 dataset, AMLP outperforms the fully supervised method by

TABLE IV: Results of our ablation studies on the Heckter and BraTS2018 datasets with 5% and 10% labelled data.

	Methods	**Hecktor**				**BraTS2018**							
	Modality	CT		PET		T1CE		T2		FLAIR		T1	
	Metrics	DSC↑	HD95↓	DSC↑	HD95↓	DSC↑	HD95↓	DSC↑	HD95↓	DSC↑	HD95↓	DSC↑	HD95↓
5%	Sup	0.1740	62.7115	0.5452	69.0963	0.3234	55.0727	0.3952	47.4584	0.4035	33.2086	0.1743	59.5963
	BASE	0.2373	61.2351	0.5692	62.3420	0.5307	53.7239	0.4152	45.2062	0.4401	32.6258	0.2486	57.7398
	MPS	0.2679	60.0462	0.5921	58.6432	0.5501	51.3462	0.4396	43.6237	0.4581	30.9462	0.2791	55.0862
	AMR	0.2512	61.2337	0.5834	60.7285	0.5425	52.6132	0.4285	44.9625	0.4423	31.4195	0.2673	56.6478
	CRCL	0.2481	60.7930	0.5802	61.1427	0.5399	52.0410	0.4205	44.8291	0.4471	30.4632	0.2578	56.9203
	MPS-AMR	0.2831	58.6127	0.6244	43.4581	0.5752	45.4307	0.4693	**40.4502**	0.4687	28.4192	0.3143	50.9173
	MPS-CRCL	0.2804	59.3581	0.6114	51.2614	0.5637	48.7651	0.4563	41.5846	0.4649	29.6834	0.3062	52.3516
	AMR-CRCL	0.2816	60.0574	0.6044	55.8031	0.5580	50.0917	0.4409	42.9724	0.4600	30.1734	0.2916	53.4329
	AMLP(Ours)	**0.2905**	**57.2823**	**0.6296**	**40.5376**	**0.5762**	**44.2326**	**0.4721**	40.6362	**0.4693**	**28.2352**	**0.3297**	**50.2342**
10%	Sup	0.2541	64.0604	0.5769	41.8627	0.4451	50.9107	0.4288	43.9483	0.4489	30.4918	0.2476	52.8203
	BASE	0.3006	58.2945	0.5932	49.6235	0.5892	47.6230	0.4518	40.4253	0.4599	29.0526	0.3351	45.2526
	MPS	0.3318	55.4185	0.6079	47.2145	0.6067	32.4192	0.4827	31.2364	0.4823	27.2345	0.3576	35.4273
	AMR	0.3187	57.6234	0.5958	48.5263	0.5903	41.5234	0.4735	38.6234	0.4748	28.9632	0.3469	39.9634
	CRCL	0.3105	57.7369	0.5960	49.1352	0.5883	45.8265	0.4693	39.6515	0.4701	28.5238	0.3390	41.3282
	MPS-AMR	0.3671	46.5192	0.6303	37.4192	0.6332	22.3254	0.5157	24.2163	0.4967	25.4163	0.3807	24.2154
	MPS-CRCL	0.3532	50.2356	0.6221	39.7684	0.6256	26.5163	0.5012	27.3175	0.4912	26.4192	0.3732	29.6234
	AMR-CRCL	0.3481	51.3252	0.6185	42.4560	0.6185	30.5124	0.4976	30.2864	0.4891	27.4258	0.3701	30.5128
	AMLP(Ours)	**0.3690**	**44.2361**	**0.6314**	**35.3453**	**0.6343**	**20.3453**	**0.5194**	**23.2375**	**0.4971**	**25.1484**	**0.3815**	**23.5632**

TABLE V: Results of loss-based ablation studies on the Hecktor and BraTS2018 datasets with 5% labeled data.

Losses	**Hecktor**				**BraTS2018**							
	CT		**PET**		**T1CE**		**T2**		**FLAIR**		**T1**	
	DSC↑	HD95↓	DSC↑	HD95↓	DSC↑	HD95↓	DSC↑	HD95↓	DSC↑	HD95↓	DSC↑	HD95↓
L_{pred}	0.2373	61.2351	0.5692	62.3420	0.5307	53.7239	0.4152	45.2062	0.4401	32.6258	0.2486	57.7398
$L_{pred}+L_{rrl}$	0.2863	59.2341	0.6152	49.2341	0.5752	47.1562	0.4673	42.1345	0.4617	29.9632	0.3187	53.2635
$L_{pred}+L_{ccl}$	0.2592	60.4562	0.5745	55.4562	0.5343	53.5263	0.4231	44.5263	0.4462	32.3526	0.2614	56.8561
$L_{pred}+L_{rrl}+L_{ccl}$ (Ours)	**0.2905**	**58.2823**	**0.6296**	**40.5376**	**0.5762**	**44.2326**	**0.4721**	**40.2362**	**0.4693**	**28.2352**	**0.3297**	**50.2342**

2.7% for DSC, 1.32% for Sen, and 0.45% for BIoU, and 0.0289 for HD95. The superior performance of AMLP can be attributed to the fact that it determines more appropriate and challenging adjustable masks for images. Reducing the uncertainty of masked patches and increasing the upper limit of conditional mutual information enables the acquisition of more comprehensive and effective representation information.

While AMLP generally excels, we also observe that its results may not always be the best in few scenarios. This can attribute to the challenge of fully capturing all informative representations with limited labeled data during self-supervised pretraining. Future research could explore the integration of attention mechanisms, such as those in [34], [35], to enhance model performance by focusing on the foreground area, potentially closing any remaining performance gaps even with limited annotations.

Analysis of visualized segmentation results. Moreover, these findings align with the visualized results in Fig. 4, where AMLP are closer to ground truth and better than other self-supervised medical image segmentation methods. A comprehensive analysis is as follows:

The contrastive methods like SimCLR, BYOL, and SwAV often lead to over-segmentation and imprecise lesion contour delineation, indicating their difficulty in preserving sharp boundaries and accurate localization due to a focus on global features. Then, the reconstruction-based approaches such as MAE, MaskFeat, and SimMIM offer finer segmentation details but still exhibit margin blurring and occasional leakage into adjacent tissues, suggesting that reconstruction alone is insufficient for precise lesion delineation. In contrast, AMLP produces segmentations closest to the ground truth, with sharper contours, and improved segmentation of small lesions, such as the enhancing ring in the T1CE slice.

This visual evidence strongly underscores AMLP's advantages, which stem from its ability to focus selectively on lesion patches and optimize representation learning, which enables the model to learn more discriminative and robust features for accurate medical image segmentation.

B. Ablation Studies

We conducted ablation studies to evaluate the effectiveness of the four key enhancements: the masked patch selection strategy, relative reconstruction loss, category consistency loss, and adjustable masking ratio. Specifically, we have implemented several models for self-supervised pretraining: (i) BASE: The BASE model is a self-supervised learning model, encompassing the pre-training upstream model (masking and reconstruction task), weight transferring, and fine-tuning of the downstream model (segmentation task). These processes are implemented based on the U-Net network. (ii) MPS: MPS incorporates only the masked patches selection strategy on the basis of BASE. (iii) AMR: AMR incorporates only the adjustable masking ratio strategy on the basis of BASE. (iv) CRCL: Combining the attention reconstruction loss and category consistency loss on the basis of BASE. (v) MPS-AMR: Integrating both the masked patches selection strategy and adjustable masking ratio strategy on the basis of BASE. (vi) MPS-CRCL: Combining the masked patches selection strategy with the joint losses (CRCL) on the basis of BASE. (vii) AMR-CRCL: Incorporating the adjustable masking ratio strategy along with the combined losses (CRCL) on the basis of BASE. (viii) AMLP (Ours): Represent the full model, incorporating all improvements on the basis of BASE.

TABLE VI: Results of different masking strategies on the Hecktor and BraTS2018 datasets with 10% labeled data.

Losses	**Hecktor**				**BraTS2018**							
	CT		**PET**		**T1CE**		**T2**		**FLAIR**		**T1**	
	DSC↑	HD95↓	DSC↑	HD95↓	DSC↑	HD95↓	DSC↑	HD95↓	DSC↑	HD95↓	DSC↑	HD95↓
random	0.3256	50.2351	0.6156	45.2365	0.6038	30.2532	0.4957	30.3209	0.4624	28.2390	0.3425	35.2624
easy to hard	0.3487	47.2630	0.6202	40.9863	0.6195	25.2263	0.5072	27.0117	0.4782	26.8805	0.3752	28.8764
hard to easy (Ours)	**0.3690**	**44.2361**	**0.6314**	**35.3453**	**0.6343**	**20.3453**	**0.5194**	**23.2375**	**0.4971**	**25.1484**	**0.3815**	**23.5632**

TABLE VII: Patches' statistical results from k-means clustering. We report the average number of patches and lesion patches over 150 samples. We found that category 1 is much better at selecting lesion patches than category 2, which verifies our motivation and model design.

	Number of patches	Number of lesion patches	Precision
category 1	15.47	7.39	47.77%
category 2	84.53	4.88	5.77%

The ablation studies are conducted on Hecktor and BraTS2018 datasets using 5% and 10% ratios of annotations, and the corresponding results are shown in Table IV. Additionally, loss ablation experiments are conducted on the two datasets with 5% labeled data to assess the effectiveness of different losses, and the results are detailed in Table V.

Effectiveness of masked patches selection. First, to verify whether k-means can effectively distinguish between foreground and background, we studied its classification precision at the beginning of the training. We randomly selected 150 samples from the BraTS2018 dataset and statistically analyzed the k-means classification results (k=2) for each sample, recording their averages in Table VII. Specifically, each sample was divided into 100 image patches of size 16×16. According to the statistical results, category 1 contains an average of 15.47 image patches, with an average of 7.39 patches being lesion patches, resulting in a classification precision of 47.77% for lesion patches in this category. Category 2 contained an average of 84.53 image patches, with an average of 4.88 patches being lesion patches, resulting in a classification precision of 5.77%. We find that the classification precision of lesion patches in category 1 is much higher than in category 2, indicating that category 1 contains more lesion patches, while category 2 mainly contains background patches. Therefore, we can use k-means as the basic method for distinguishing between foreground and background and further optimize this method during training to improve classification precision. Additionally, we observed that the number of patches in category 1 is always much smaller than in category 2. Since lesion areas in medical images occupy only a small part of the entire image, our method defaults to considering the category with fewer patches as the foreground and the category with more patches as the background.

Based on this, we further verified the effectiveness of the MPS strategy, with results shown in Table IV. The results demonstrate that MPS consistently outperforms BASE. For instance, employing only MPS in Hecktor CT with 5% labeled data increased DSC by 3.06% and reduced HD95 by 1.1889 compared to BASE. removing MPS from the complete AMR-CRCL model resulted in performance degradation with DSC decreasing by 0.89% and HD95 increasing by 2.7751. This can be attributed to MPS's targeted focus on lesion patches during reconstruction, enabling better capture of lesion texture and shape characteristics. This targeted learning approach proves particularly beneficial for medical images where lesions often present complex shapes and blurred boundaries.

Effectiveness of CRCL To evaluate the effectiveness of the combined losses, we conducted loss-based ablation studies on Hecktor and BraTS2018 datasets with 5% and 10% labeled data. The combined losses refer to the relatvie reconstruction loss L_{rrl} and category consistency loss L_{ccl}. Since L_{ccl} depends on the MPS, so it is excluded when evaluating the part that does not contain MPS.

As shown in Table V, the results show that using L_{rrl} or L_{ccl} alone can improve model performance. In the Hecktor CT modality with 5% labeled data, using L_{rrl} alone can improve DSC by 4.9%, and using L_{ccl} alone can reduce HD96 by 0.7789. This is because L_{rrl} can help model focus on lesion area accurately, and L_{ccl} can alleviate the misclassification problem of unsupervised k-means and enhance the model's ability to distinguish between foreground and background. At the same time, we also found that the combination of L_{rrl} and L_{ccl} can further improve model performance.

Effectiveness of adjustable masking ratio. Besides, as shown in Table IV, we can observe that the results of AMR is generally better than BASE. For instance, using AMR on BraTS2018 T1 with 5% labeled data increased DSC by 1.87% and reduced HD95 by 1.092. And by removing AMR from the whole model, which is CCL(-MPS-RRL), we can also see the results of DSC reduce by 2.35% and HD95 for 2.1174. This boost results from AMR's adjustable masking schedule, promoting continuous representation learning, facilitating the acquisition of richer and more diverse representations.

Effectiveness of masking strategies. Furthermore, to verify the effectiveness of masking strategy, we design additional ablation study in Table VI. Specifically, we compare three kinds of masking strategies: (i) random masking: randomly mask image patches. (ii) easy to hard: preferentially mask background patches, then gradually increase masking ratio. (iii) hard to easy: preferentially mask lesion patches, then gradually increase masking ratio.

The results shows that the performance of "hard to easy" is superior to "easy to hard", with "random" yielding the poorest result, indicating that masking lesion areas firstly leads to better performance than masking background. For example, in the Hecktor CT mode with 10% labeled data, the DSC result of "hard to easy" is 2.03% higher than that of "easy to hard" and 4.34% higher than "random". This improvement can be attributed to the fact that lesion areas contain critical information necessary for accurate segmentation. By focusing on masking these regions first, the model is forced to learn

TABLE VIII: The DSC results of different clustering methods achieved by AMLP on T1 modality of BraTS2018 with 10% labeled data.

methods	k-means	hierarchical	t-SNE	DBSCAN
DSC	0.3815	0.3659	0.3894	0.3770
Complexity	$O(n)$	$O(n^2)$	$O(n^2)$	$O(n^2)$

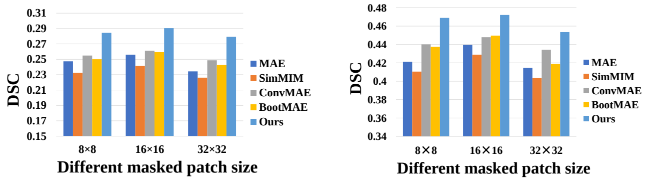

(a) Hecktor dataset (b) BraTS2018 dataset

Fig. 5: Compare the DSC segmentation results of the proposed AMLP and other MIM methods on different masked patch sizes on the CT modality of Hecktor and T2 modality of BraTS2018 datasets with 5% labeled data.

more robust and discriminative features to handle the most challenging parts of the image. Simultaneously, this strategy is also consistent with the typical diagnostic process, where radiologists typically first examine the lesion and then consider the condition of the surrounding tissues. On the other hand, starting with background masking might lead to less informative learning initially, as the background regions generally contain less complex features compared to lesions. Random masking, lacking any strategic prioritization, results in the worst performance, highlighting the importance of a well-thought-out masking strategy in training effective models.

C. Additional Experiments

Analysis of different clustering methods. To determine the optimal clustering approach for lesion segmentation, we evaluated four prevalent unsupervised methods on AMLP and T1 modality of BraTS2018 dataset with 10% labeled data: k-means, hierarchical clustering, t-SNE and DBSCAN. As shown in Table VIII, the DSC k-means achieved is 0.3815. This result was only 0.79% lower than the best score of 0.3894 attained by t-SNE. However, k-means held a significant advantage in computational complexity, with a time complexity of $O(n)$ compared to $O(n^2)$ for other methods. The combination of strong performance approaching the optimum score with low complexity highlights k-means as an efficient and effective choice compatible with the hardware and time constraints of real-world clinical deployment. Compared to hierarchical and density-based clustering, k-means provides a favorable trade-off between accuracy and efficiency critical for practical utility.

Analysis of different masked patch sizes. Furthermore, in order to explore the impact of patch size on model performance and to find the most suitable patch size for medical image analysis tasks, we conducted additional experiment to compare the DSC performance of AMLP and other baselines using different masked patch size of 8×8, 16×16 (used in our paper) and 32×32 on the CT modality of Hecktor dataset and T2 modality of BraTS2018 dataset with 5% labeled data. Results are shown in Fig. 5. The results indicates that our proposed AMLP outperforms other baselines across different masked patch sizes on both datasets, demonstrating the effectiveness of our proposed AMLP in medical image segmentation task. Additionally, all methods achieve the best performance with the masked patch of 16x16, suggesting that a moderate patch size is optimal in MIM methods. This is because smaller patch sizes may cause the model to learn too many short connections, and too many corresponding hints from smaller visible patches may limit the improvement in generalization ability. On the other hand, larger masked patch size may enforce the network to learn relatively long-range connections and make the learning process too difficult.

TABLE IX: DSC results with different pre-set misclassification ratios on the T2 modality of BraTS2018 using 10% labeled data. "w/ updated patch labels" means the pre-classified incorrect label categories updates with the training process. "w/o updated patch labels" means unchanged.

pre-set misclassification ratio	0%	10%	20%	30%
w/ updated patch labels	0.5194	0.5150	0.5103	0.4975
w/o updated patch labels	0.5194	0.5059	0.4932	0.4740

Analysis of tolerance for misclassification. To validate our proposed model's ability to correct initial misclassifications, we have conducted pre-set misclassification ratios experiments as shown in "w/ updated patch labels" of Table IX. Specifically, before training commenced, we deliberately set a fixed proportion (0%, 10%, 20%, and 30%) of misclassified image patches in the input to the network, allowing the network to update the class labels of all image patches during training. We then tested the model's segmentation performance. The results indicate that the DSC for the cases with 10% and 20% pre-misclassified patches only differed by 0.44% and 0.91%, respectively, from the 0% misclassification scenario. This suggests that the model can correct initial misclassifications to some extent. However, when the pre-misclassification rate reached 30%, the performance difference compared to 0% misclassification increased to 2.19%, highlighting the potential impact of misclassification rates on model performance.

Additionally, to investigate our method's tolerance to misclassification, we conducted experiments where the proportion of misclassified patches was also fixed throughout the training process, meaning that the network could not update the class labels of these pre-misclassified patches. The results, shown in Table IX under the "w/o updated patch labels" condition, reveal that the performance with a 10% initial misclassification rate differed from the 0% rate by only 1.35%. This indicates that even with 10% of patches misclassified, the performance loss is relatively limited, demonstrating the model's tolerance to misclassification. However, when the predetermined misclassification rates reached 20% or 30%, the DSC differences compared to 0% were 2.62% and 4.54%, respectively. This shows that the model's tolerance decreases as the misclassification rate increases.

However, when verifying the effectiveness of k-means, we previously found that even an untrained k-means algorithm has a maximum misclassification rate of approximately 12.96% for foreground-background classification, as shown in Table VII. This means that our model is highly unlikely to encounter

TABLE X: Comparison of DSC segmentation results for each single hierarchical label in the T1CE modality of the BraTS2018 dataset with 5% labeled data. Among them, WT represents the whole tumor, TC represents the tumor core, ET represents the enhancing tumor, and Avg. indicates the mean DSC of the segmentation results for the three categories.

Methods	ET	WT	TC	Avg.
SimCLR	0.4299	0.6540	0.5370	0.5403
BYOL	0.4085	0.6391	0.5259	0.5245
SwAV	0.4301	0.6215	0.5240	0.5252
MAE	0.4337	0.6667	0.5391	0.5465
SimMIM	0.4181	0.6797	0.5285	0.5421
ConvMAE	0.4172	0.7276	0.5208	0.5552
BootMAE	0.4133	0.7211	0.4949	0.5431
SelfMedMAE	0.4214	0.7182	0.5173	0.5523
Ours	**0.4476**	**0.7351**	**0.5459**	**0.5762**

TABLE XI: Performance comparison between AMLP and No New-Net under varying proportions of labeled data and different backbone architectures.

Methods	DSC
AMLP (50%, 2D U-Net,)	0.7545
AMLP (100%, 2D U-Net)	0.8376
No New-Net (100%, 3D U-Net) [36]	0.8210
AMLP (100%, 3D U-Net)	0.8513

a misclassification rate as high as 20% or 30%, but rather around 10% or even lower. Therefore, our model has sufficient corrective ability and fault tolerance in most cases, ensuring the stability of our model's performance.

Analysis of single hierarchical labels segmentation. We further present all three single-class DSC results of T1CE modality from BraTS2018 dataset in Table X. With 5% labeled data, our method not only outperforms the average results of three levels of labels but also consistently surpasses other methods in all single tumor categories. Specifically, our method achieves 1.39%, 0.75%, and 0.68% better DSC in the segmentation of WT, TC, and ET structures, respectively, compared to the second-best results. This is attributed to our method's stronger ability to distinguish between lesion and background areas, leading to more accurate results in various lesion edge segmentations.

Analysis of multimodality. Theoretically, combining multiple modalities provides complementary visual information to the model, which can help capture the anatomical and pathological features present in medical images more comprehensively and accurately. To this end, besides training on single modalities for BraTS (T1CE, T2, Flair, and T1), we also conducted a new set of experiments where all four modalities were used as input for training simultaneously.

Specifically, we first compared the performance of the proposed AMLP and various self-supervised segmentation methods when all four modalities were used as input for training simultaneously. As shown in Fig. 6 (a), our proposed model maintained the best performance under 5%, 10%, and 50% annotation ratios when trained with all four modalities, demonstrating the effectiveness of our method. Subsequently, we further investigated the performance difference between training with all four modalities simultaneously and training with each of the four modalities individually. As shown in Fig. 6 (b), the method of training with all four modalities simultaneously achieved much higher performance than single-modality training across various annotation ratios, indicating that multimodality combination can indeed significantly enhance the model's ability to recognize complex lesions. Therefore, in future work, we will continue to explore strategies for multimodality information fusion to further improve the model's robustness and adaptability.

TABLE XII: Comparison of results for normal organ segmentation on the ABD110 dataset with 10% labeled data.

Methods	U-Net	MoCo	DenseCL	G-L	MAE	MaskFeat	Ours
DSC	0.7438	0.8135	0.8107	0.8139	0.7767	0.7639	0.8315

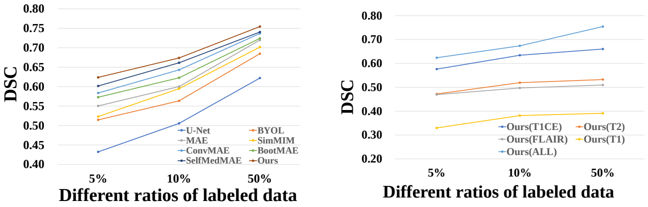

(a) Various methods trained with multimodal data (b) Our method trained with different modalities data

Fig. 6: Performance comparison of the model using multi-modalities of BraTS2018 with different annotation ratios.

We also noted that the multimodal segmentation results in Fig. 6 are not as high as those reported for the BraTS dataset in other papers (e.g., those in [36]). This is because our work is based on a self-supervised approach, where only a certain proporition of the data has segmentation labels. In contrast, many multimodal segmentation studies are conducted in a fully-supervised setting, utlizing complete segmentation annotation for all data. Additionally, we employ a different backbone model from some works (e.g., [36] uses 3D U-Net, while we use 2D U-Net). Therefore, to demonstrate the superior performance of our proposed AMLP method for multi-modal segmentation and to prevent an underestimation of its capabilities due to setup discrepancies, we use [36] as a baseline and evaluate AMLP in a fully-supervised setting, with both 2D-UNet and 3D-UNet as backbones. The results are presented in Table XI. We can observe that under the same 3D U-Net and 100% labeled data, our model achieves 0.8513, surpassing No New-Net by 0.303. This result robustly demonstrates AMLP imparts a substantial and inherent advantage, enabling the learning of more effective representations.

Analysis of normal anatomical structures segmentation tasks. Although the components of AMLP were originally designed for the lesion segmentation scenario, their working mechanism gives them the potential to handle a wider range of medical image analysis tasks. For example, MPS operates based on the principle of binary classification in feature space, which is not only suitable for segmenting lesion and non-lesion areas, but also for segmenting organs and background. RRL and CCL focus on extracting and optimizing unique feature representations of target categories, regardless of whether they are lesions or organs.

TABLE XIII: Detection results of the proposed method and baselines on FLAIR modality of BraTS2018 and RSNA Pneumonia dataset with 10% labeled data.

Methods		BraTS2018				RSNA Pneumonia			
		AP_{50}	AP_{70}	R_{50}	R_{70}	AP_{50}	AP_{70}	R_{50}	R_{70}
10%	Faster-RCNN	0.4301	0.1567	0.4978	0.1929	0.384	0.0991	0.5052	0.2129
	BYOL	0.4523	0.2105	0.5163	0.2647	0.3911	0.0997	0.5062	0.2159
	MAE	0.4772	0.2361	0.5451	0.2854	0.3937	0.1016	0.5104	0.2260
	ConvMAE	0.4904	0.2526	0.5507	0.3034	0.3945	0.1023	0.5165	0.2321
	Ours	**0.5281**	**0.2812**	**0.5763**	**0.3345**	**0.4107**	**0.1045**	**0.5211**	**0.2354**
50%	Faster-RCNN	0.5319	0.3057	0.5909	0.3684	0.4023	0.1055	0.5239	0.2287
100%	Faster-RCNN	0.6045	0.3821	0.6792	0.4593	0.4789	0.1241	0.6313	0.2629

TABLE XIV: Hyperparameter configuration for model training.

config	value
optimizer	[SGD, Adam, AdamW]
base learning rate	[1e-5, 1e-4, 1e-3]
weight decay	[0.005, 0.01, 0.05, 0.1]
optimizer momentum	β_1; β_2=0:9; 0:95
batch size	512
learning rate schedule	cosine decay
warmup epochs	[20, 40, 60]
training epochs	[400, 800, 1200, 1600]
augmentation	RandomResizedCrop

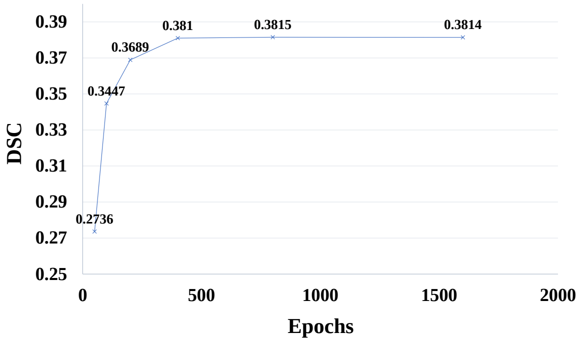

Fig. 7: Training schedules. The DSC results of training our proposed AMLP trained at different epochs on the T1 modality of BraTS2018 dataset with 10% labeled data.

To further explore the applicability of AMLP to the normal anatomy segmentation task, we performed abdominal segmentation experiments on the publicly available ABD110 dataset with 10% labeled data. The results are shown in Table. XII. We can observe that our proposed method achieves the best performance among all methods, with a DSC 1.76% higher than the second-best result, which benefits from the model's learning of key discriminative features for distinguishing anatomical regions from backgrounds. These results indicate that our proposed method can be used not only for lesion segmentation tasks, but also for normal anatomy segmentation tasks.

Hyperparameters for pre-training. To ensure the robustness and reproducibility of our results, we performed a systematic hyperparameter optimization for the pre-training stage. We employed a step-wise grid search methodology, and the search space for key hyperparameters is detailed in Table XIV, with the final optimal configuration underlined. Our search results reveal that the AdamW optimizer, combined with a learning rate of 1e-4 and a weight decay of 0.05, yielded the most effective feature representations for downstream tasks. All results are the average of three independent runs using this optimal setup. Furthermore, we have evaluated the performance of training duration, as shown in Fig. 7. The downstream performance (DSC) on the BraTS2018 T1 modality (10% labels) plateaus around 800 epochs, indicating that longer training provides diminishing returns and risks overfitting to the pre-training task. We thus selected 800 epochs as the optimal trade-off between performance and efficiency.

Analysis of detection task. In order to more comprehensively demonstrate AMLP's ability to learn and represent lesion features, as well as its wide impact and applicability to downstream tasks, we have conducted additional medical image lesion detection experiments.

Specifically, we verified the performance of AMLP on detection task with the public BraTS [29] and RSNA Pneumonia [37] detection dataset. BraTS detection dataset is converted from the FLAIR modality of BraTS segmentation dataset, where segmentation labels are converted to detection labels. RSNA Pneumonia detection dataset is a public medical imaging dataset for pneumonia detection created by the Radiological Society of North America (RSNA). In order to better evaluate the performance of AMLP in detection tasks, we used the most widely used average precision (AP) and Recall (R) as evaluation indicators. The detection results of AMLP at different annotation ratios are compared with contrastive learning method (BYOL [11]), the masked image modeling method (MAE [18] , ConvMAE [21]), and Faster-RCNN [38] as shown in Table XIII.

As observed, various self-supervised methods outperform Faster R-CNN in detection accuracy when using only 10% labeled data. Additionally, our proposed AMLP method achieved the best performance among all self-supervised methods, nearing the performance of Faster R-CNN detection model at 50% annotation. On BraTS dataset, compared to the second-best baseline method, AMLP achieved 3.77% better results on AP_{50} and 2.56% better results on R_{50}. On RSNA Pneumonia detection dataset, AMLP outperformed the second-best baseline by 1.62% on AP_{50} and 0.46% on R_{50}. These findings strongly indicate that our method has successfully generalized in the task of lesion detection. AMLP learns more discriminative features from masked lesions, which significantly benefits the detection task.

Extensibility to Different Backbones. To validate the applicability of our strategy on different architectures and di-

TABLE XV: Comparison of 2D and 3D segmentation methods on the BraTS2018 multimodal dataset.

	Backbone	Method	Metrics	
			DSC ↑	HD95 ↓
2D	CNN	MAE (U-Net), w/o ours	0.8182	7.47
		MAE (U-Net), w/ ours	0.8376	6.26
	Transformer	MAE (ViT), w/o ours	0.8103	9.24
		MAE (ViT), w/ ours	0.8309	7.32
		SimMIM (Swin), w/o ours	0.8250	7.27
		SimMIM (Swin), w/ ours	0.8414	5.62
	Mamba	U-Mamba, w/o ours	0.8495	6.93
		U-Mamba, w/ ours	0.8662	5.72
3D	CNN	MAE (3D U-Net), w/o ours	0.8337	7.29
		MAE (3D U-Net), w/ ours	0.8513	5.63
	Transformer	SelfMedMAE (ViT), w/o ours	0.8294	8.06
		SelfMedMAE (ViT), w/ ours	0.8481	6.22
		ConvMAE (CNN+Trans.), w/o ours	0.8325	7.84
		ConvMAE (CNN+Trans.), w/ ours	0.8502	6.71
	Mamba	SegMamba, w/o ours	0.8505	5.63
		SegMamba, w/ ours	0.8756	4.74

TABLE XVI: Comparison of efficiency between vision foundation models and AMLP on the BraTS2018 multimodal dataset.

Methods	AMLP	SAM	SAM v2	Med-SAM	MA-SAM	3D SAM-Adapter
Total Parameters (M)	31	636	224	95	97	102.4
Inference Peak Memory (GB)	0.4	5.2	3.5	2.3	2.4	8.7

TABLE XVII: Comparison of segmentation results of vision foundation models and AMLP on BraTS2018 multimodal dataset.

Methods	Initialization weights	DSC↑	BIoU↑
AMLP (50%)	–	0.7545	0.3713
AMLP (100%)	–	0.8376	0.4782
SAM	ViT-H	0.7422	0.3881
SAM v2	Hiera-L	0.7610	0.4079
MedSAM	MedSAM-ViT-B	0.8067	0.4505
MA-SAM	SAM-ViT-B	0.8010	0.4474
MA-SAM	MedSAM-ViT-B	0.8125	0.4570
3D SAM-Adapter	SAM-ViT-B	0.8153	0.4592
3D SAM-Adapter	MedSAM-ViT-B	0.8271	0.4682

mensionality settings, besides using U-Net as the backbone, we have also conducted comprehensive experiments across different backbones including 2D and 3D and various architectures including CNN-based (U-Net [31], 3D U-Net [39]), transformer-based (MAE [18], SimMIM [19], SelfMedMAE [15], ConvMAE [21]), and the recent Mamba-based models (U-Mamba [40], SegMamba [41]). The results are shown in Table XV. We can observe that our proposed method (*w/ ours*) consistently outperforms the baseline (*w/o ours*) across all evaluated architectures. Specifically, we observe a notable increase in DSC (nearly 2% on average) and a reduction in HD95 (about 1.5 on average). These consistent improvements across CNN-based, transformer-based, and Mamba-based architectures, in both 2D and 3D formulations, validate the effectiveness and robustness of our SSL strategy.

Comparing with Vision Foundation Models. As the vision foundation models emerge, we also want to know the performances of our AMLP model comparing to the existing vision foundation models, e.g, SAM [42], SAM v2 [43], Med-SAM [44], MA-SAM [45] and 3D SAM-Adapter [46]. However, Firstly, the large model is pre-trained with a large number of images of various types (e.g., 11 million images for SAM), while our model is training from scratch with only hundreds of cases in total, so they have a huge difference in terms of training data; Secondly, the vision foundation models have a large number of parameters, and their training is very computationally and memory-intensive and time-consuming; Therefore, it is very unfair to directly compare the segmentation results obtained by our self-supervised training based on only 10% of the labeled data with the results of the medical segmentation foundation models trained with massive data. Therefore, we adjust our model training settings and train AMLP using multimodal BRATS data with 50% and 100% annotations respectively, so as to try to bridge the data gap between AMLP and the foundation models, and then compare the performance differences between AMLP and the large model under these settings.

As shown in Table XVII, our AMLP outperforms all five vision foundation models with 100% labeled data. For example, with 100% labels, AMLP outperforms MA-SAM (based on SAM-ViT-B initialization weights) by 3.66% in DSC, and 3.08% in BIoU. Besides, we also compare with MA-SAM [45] and 3D SAM-Adapter [46] initialized with MedSAM-ViT-B weights [44]: AMLP outperforms MA-SAM with MedSAM-ViT-B by 2.51% in DSC and 2.12% in BIoU; while outperforming 3D SAM-Adapter by 1.05% in DSC and 1.00% in BIoU. Even with 50% of labeled data, AMLP remains competitive with baselines like Med-SAM [44]. This indicates that, with sufficient domain-specific data, our specific pre-training strategy attains segmentation accuracy comparable to or better than directly using or parameter-efficiently adapting generalist foundation models. Furthermore, as shown in Table XVI, our proposed AMLP has only 31 MB total parameters and 0.4 GB inference peak memory. The parameters of foundation models are 3 or even 20 times that of AMLP, and inference peak memory is 6 or even 22 times that of AMLP. Besides, replacing the SAM-ViT-B weights with MedSAM-ViT-B for MA-SAM and 3D SAM-Adapter does not change the number of parameters and inference peak memory, because they use the same SAM ViT-B backbone. In conclusion, our AMLP model can achieve better segmentation results with limited computational resources.

V. Discussion and future work

A. Social impact for proposed algorithm

The proposed model has wide-ranging applications in daily clinical scenarios, significantly reducing the burden on specialists while safeguarding diagnostic precision. For example, in cancer radiotherapy, precisely delineating tumors in 3D CT or PET scans often requires hours of slice-by-slice annotation and the collaboration of multiple physicians—a task that consumes limited human resources and extends patient waiting times for treatment. In this context, our method can generate a high-quality initial contour in seconds, allowing clinicians to then refine the lesion, thereby streamlining the clinical annotation workflow. Similarly, in multi-parametric brain magnetic resonance imaging (MRI), our network can generate high-fidelity glioma boundaries to assist neurosurgeons in designing minimally invasive surgical trajectories, thus accelerating the entire treatment planning process.

Furthermore, our self-supervised framework achieves precise segmentation without the high annotation costs of fully supervised methods. This greatly reduces the data requirements for automated medical image segmentation systems in clinical settings, helps improve their deployment efficiency, and ultimately lowers patient examination costs in specific clinical scenarios.

B. Limitations and future work

Although our proposed AMLP solves the problem of MIM application deviation in natural images and medical images to a certain extent. It still have some improvement space. For instance, we can significantly improve the mask selection strategy by integrating domain-specific expertise and prior knowledge from the field of medicine. This could involve considering prevalent lesion locations associated with various diseases and accounting for the distinct morphological characteristics exhibited by different types of lesions. Employing such tailored mask selection techniques holds substantial promise in enhancing the model's ability to discern between various diseases and lesions, thus contributing to the overall improvement of medical image segmentation.

While our method demonstrates superior performance in comparison to existing self-supervised methods, there remains a little performance gap when comparing to fully supervised methods. It can potentially be addressed through incorporation of more advanced techniques like reinforcement learning [47], [48]. Specifically, the mask selection process can be conceptualized as a Markov decision process, enabling adaptive optimization through policy gradient methods. This approach may provide a more effective solution.

Moreover, although we have trained our model on various datasets encompassing different modalities (such as CT and MRI) and anatomical regions (such as head and neck cancer, and brain tumors), its performance may not maintain the same level of stability and accuracy when transferred to heterogeneous datasets with different sources (e.g., from different institutions or acquired using different equipment) or with inconsistent feature distributions. This limitation may lead to suboptimal performance when the model encounters unseen data, thereby affecting its applicability and robustness in broader clinical environments. Therefore, future research should incorporate more diverse datasets and employ techniques such as transfer learning to enhance the model's generalization capabilities and improve its adaptability across different application scenarios.

In summary, combining cross-knowledge with deep learning methods stands as a key direction for future medical image segmentation research. Such integrated approaches have potential to enhance model performance, and provide more reliable support for patient health.

VI. Conclusion

In this paper, we proposed a self-supervised framework named Adjustable Masked Lesion Patches (AMLP) for medical image segmentation. This architecture can leverage unlabeled medical images for representation learning by masking and reconstructing lesion patches. Specifically, under the guidance of the masked patch selection strategy, the model can focus on learning informative representations of important lesion areas. In addition, we designed an relative reconstruction loss and category consistency loss, which can strengthen the model's focus on lesions patches and enhance distinction between lesions and background. Moreover, we developed an adjustable masking ratio strategy that gradually increases the masking ratio over training to expand the scope of learnable mutual information. Through extensive experiments on two public datasets, we illustrate that our method can achieve remarkable performance with only a small portion of annotations. This capability substantially enhances the utilization of the wealth of unlabeled medical images.

References

[1] Z. Xu, S. Liu, D. Yuan, L. Wang, J. Chen, T. Lukasiewicz, Z. Fu, and R. Zhang, "ω-Net: Dual supervised medical image segmentation with multi-dimensional self-attention and diversely-connected multi-scale convolution," *Neurocomputing*, vol. 500, pp. 177–190, 2022.

[2] K. Kamnitsas, C. Ledig, V. F. Newcombe, J. P. Simpson, A. D. Kane, D. K. Menon, D. Rueckert, and B. Glocker, "Efficient multi-scale 3D CNN with fully connected CRF for accurate brain lesion segmentation," *Medical Image Analysis*, vol. 36, pp. 61–78, 2017.

[3] D. Yuan, Z. Xu, B. Tian, H. Wang, Y. Zhan, and T. Lukasiewicz, "μ-Net: Medical image segmentation using efficient and effective deep supervision," *Computers in Biology and Medicine*, vol. 160, p. 106963, 2023.

[4] J. Zhang, S. Zhang, X. Shen, T. Lukasiewicz, and Z. Xu, "Multi-ConDoS: Multimodal contrastive domain sharing generative adversarial networks for self-supervised medical image segmentation," *IEEE Transactions on Medical Imaging*, vol. 43, no. 1, pp. 76–95, 2024.

[5] X. Chen, M. Ding, X. Wang, Y. Xin, S. Mo, Y. Wang, S. Han, P. Luo, G. Zeng, and J. Wang, "Context autoencoder for self-supervised representation learning," *International Journal of Computer Vision*, pp. 1–16, 2023.

[6] D. Shen, G. Wu, and H.-I. Suk, "Deep learning in medical image analysis," *Annual Review of Biomedical Engineering*, vol. 19, pp. 221–248, 2017.

[7] G. Litjens, T. Kooi, B. E. Bejnordi, A. A. A. Setio, F. Ciompi, M. Ghafoorian, J. A. Van Der Laak, B. Van Ginneken, and C. I. Sánchez, "A survey on deep learning in medical image analysis," *Medical Image Analysis*, vol. 42, pp. 60–88, 2017.

[8] S. Zhang, J. Zhang, B. Tian, T. Lukasiewicz, and Z. Xu, "Multi-modal contrastive mutual learning and pseudo-label re-learning for semi-supervised medical image segmentation," *Medical Image Analysis*, vol. 83, p. 102656, 2023.

[9] T. Chen, S. Kornblith, M. Norouzi, and G. Hinton, "A simple framework for contrastive learning of visual representations," in *Proceedings of ICML*, 2020, pp. 1597–1607.

[10] K. He, H. Fan, Y. Wu, S. Xie, and R. Girshick, "Momentum contrast for unsupervised visual representation learning," in *Proceedings of CVPR*, 2020, pp. 9729–9738.

[11] J.-B. Grill, F. Strub, F. Altché, C. Tallec, P. Richemond, E. Buchatskaya, C. Doersch, B. Avila Pires, Z. Guo, M. Gheshlaghi Azar *et al.*, "Bootstrap your own latent-a new approach to self-supervised learning," *Advances in Neural Information Processing Systems*, vol. 33, pp. 21 271–21 284, 2020.

[12] M. Caron, I. Misra, J. Mairal, P. Goyal, P. Bojanowski, and A. Joulin, "Unsupervised learning of visual features by contrasting cluster assignments," *Advances in Neural Information Processing Systems*, vol. 33, pp. 9912–9924, 2020.

[13] K. Chaitanya, E. Erdil, N. Karani, and E. Konukoglu, "Contrastive learning of global and local features for medical image segmentation with limited annotations," *Advances in Neural Information Processing Systems*, vol. 33, 2020.

[14] H.-Y. Zhou, C. Lu, S. Yang, X. Han, and Y. Yu, "Preservational learning improves self-supervised medical image models by reconstructing diverse contexts," in *Proceedings of ICCV*, 2021, pp. 3499–3509.

[15] M. Goncharov, V. Soboleva, A. Kurmukov, M. Pisov, and M. Belyaev, "vox2vec: A framework for self-supervised contrastive learning of voxel-level representations in medical images," in *Proceedings of MICCAI*, 2023, pp. 605–614.

[16] H. Li, Y. Ouyang, and X. Wan, "Self-supervised alignment learning for medical image segmentation," *Proceedings of ISBI*, pp. 1–5, 2024.

[17] M. Seince, L. L. Folgoc, L. A. F. de Souza, and E. Angelini, "Dense self-supervised learning for medical image segmentation," *Proceedings of MIDL*, pp. 1–5, 2024.

[18] K. He, X. Chen, S. Xie, Y. Li, P. Dollár, and R. Girshick, "Masked autoencoders are scalable vision learners," in *Proceedings of CVPR*, 2022, pp. 16 000–16 009.

[19] Z. Xie, Z. Zhang, Y. Cao, Y. Lin, J. Bao, Z. Yao, Q. Dai, and H. Hu, "Simmim: A simple framework for masked image modeling," in *Proceedings of CVPR*, 2022, pp. 9653–9663.

[20] C. Wei, H. Fan, S. Xie, C.-Y. Wu, A. Yuille, and C. Feichtenhofer, "Masked feature prediction for self-supervised visual pre-training," in *Proceedings of CVPR*, 2022, pp. 14 668–14 678.

[21] P. Gao, T. Ma, H. Li, J. Dai, and Y. Qiao, "Convmae: Masked convolution meets masked autoencoders," *arXiv preprint arXiv:2205.03892*, 2022.

[22] Z. Peng, L. Dong, H. Bao, Q. Ye, and F. Wei, "Beit v2: Masked image modeling with vector-quantized visual tokenizers," *arXiv preprint arXiv:2208.06366*, 2022.

[23] X. Dong, J. Bao, T. Zhang, D. Chen, W. Zhang, L. Yuan, D. Chen, F. Wen, and N. Yu, "Bootstrapped masked autoencoders for vision bert pretraining," in *Proceedings of ECCV*, 2022, pp. 247–264.

[24] L. Zhou, H. Liu, J. Bae, J. He, D. Samaras, and P. Prasanna, "Self pre-training with masked autoencoders for medical image classification and segmentation," in *Proceedings of ISBI*, 2023, pp. 1–6.

[25] X. Li, W. Wang, L. Yang, and J. Yang, "Uniform masking: Enabling mae pre-training for pyramid-based vision transformers with locality," *arXiv preprint arXiv:2205.10063*, 2022.

[26] I. Kakogeorgiou, S. Gidaris, B. Psomas, Y. Avrithis, A. Bursuc, K. Karantzalos, and N. Komodakis, "What to hide from your students: Attention-guided masked image modeling," in *Proceedings of ECCV*, 2022, pp. 300–318.

[27] N. Dhanachandra, K. Manglem, and Y. Jina Chanu, "Image segmentation using k -means clustering algorithm and subtractive clustering algorithm," *Procedia Computer Science*, vol. 54, pp. 764–771, 2015.

[28] Y. Yuan, "Automatic head and neck tumor segmentation in PET/CT with scale attention network," in *Proceedings of the 3D Head and Neck Tumor Segmentation in PET/CT Challenge*, 2020, pp. 44–52.

[29] B. H. Menze, A. Jakab, S. Bauer, J. Kalpathy-Cramer, K. Farahani, J. Kirby, Y. Burren, N. Porz, J. Slotboom, R. Wiest *et al.*, "The multimodal brain tumor image segmentation benchmark (BRATS)," *IEEE Transactions on Medical Imaging*, vol. 34, no. 10, pp. 1993–2024, 2014.

[30] I. Loshchilov and F. Hutter, "Decoupled weight decay regularization," *arXiv preprint arXiv:1711.05101*, 2017.

[31] O. Ronneberger, P. Fischer, and T. Brox, "U-net: Convolutional networks for biomedical image segmentation," in *Proceedings of MICCAI*, 2015, pp. 234–241.

[32] L. R. Dice, "Measures of the amount of ecologic association between species," *Ecology*, vol. 26, no. 3, pp. 297–302, 1945.

[33] B. Cheng, R. Girshick, P. Dollár, A. C. Berg, and A. Kirillov, "Boundary iou: Improving object-centric image segmentation evaluation," in *Proceedings of CVPR*, 2021, pp. 15 334–15 342.

[34] Z. Xu, B. Tian, S. Liu, X. Wang, D. Yuan, J. Gu, J. Chen, T. Lukasiewicz, and V. C. M. Leung, "Collaborative attention guided multi-scale feature fusion network for medical image segmentation," *IEEE Transactions on Network Science and Engineering*, vol. 11, no. 2, pp. 1857–1871, 2024.

[35] Z. Xu, X. Zhang, H. Zhang, Y. Liu, Y. Zhan, and T. Lukasiewicz, "EFPN: Effective medical image detection using feature pyramid fusion enhancement," *Computers in Biology and Medicine*, vol. 163, p. 107149, 2023.

[36] F. Isensee, P. Kickingereder, W. Wick, M. Bendszus, and K. H. Maier-Hein, "No new-net," in *Proceedings of MICCAI*, 2019, pp. 234–244.

[37] G. Shih, C. C. Wu, S. S. Halabi, M. D. Kohli, L. M. Prevedello, T. S. Cook, A. Sharma, J. K. Amorosa, V. Arteaga, M. Galperin-Aizenberg *et al.*, "Augmenting the national institutes of health chest radiograph dataset with expert annotations of possible pneumonia," *Radiology: Artificial Intelligence*, vol. 1, no. 1, p. e180041, 2019.

[38] S. Ren, K. He, R. Girshick, and J. Sun, "Faster r-cnn: Towards real-time object detection with region proposal networks," *Advances in Neural Information Processing Systems*, vol. 28, 2015.

[39] Ö. Çiçek, A. Abdulkadir, S. S. Lienkamp, T. Brox, and O. Ronneberger, "3d u-net: learning dense volumetric segmentation from sparse annotation," in *Proceedings of MICCAI*, 2016, pp. 424–432.

[40] J. Ma, F. Li, and B. Wang, "U-mamba: Enhancing long-range dependency for biomedical image segmentation," *arXiv preprint arXiv:2401.04722*, 2024.

[41] Z. Xing, T. Ye, Y. Yang, G. Liu, and L. Zhu, "Segmamba: Long-range sequential modeling mamba for 3d medical image segmentation," in *Proceedings of MICCAI*, 2024, pp. 578–588.

[42] A. Kirillov, E. Mintun, N. Ravi, H. Mao, C. Rolland, L. Gustafson, T. Xiao, S. Whitehead, A. C. Berg, W.-Y. Lo *et al.*, "Segment anything," in *Proceedings of ICCV*, 2023, pp. 4015–4026.

[43] N. Ravi, V. Gabeur, Y.-T. Hu, R. Hu, C. Ryali, T. Ma, H. Khedr, R. Rädle, C. Rolland, L. Gustafson *et al.*, "Sam 2: Segment anything in images and videos," *arXiv preprint arXiv:2408.00714*, 2024.

[44] J. Ma, Y. He, F. Li, L. Han, C. You, and B. Wang, "Segment anything in medical images," *Nature Communications*, vol. 15, no. 1, p. 654, 2024.

[45] C. Chen, J. Miao, D. Wu, A. Zhong, Z. Yan, S. Kim, J. Hu, Z. Liu, L. Sun, X. Li *et al.*, "Ma-sam: Modality-agnostic sam adaptation for 3d medical image segmentation," *Medical Image Analysis*, vol. 98, p. 103310, 2024.

[46] S. Gong, Y. Zhong, W. Ma, J. Li, Z. Wang, J. Zhang, P.-A. Heng, and Q. Dou, "3dsam-adapter: Holistic adaptation of sam from 2d to 3d for promptable tumor segmentation," *Medical Image Analysis*, vol. 98, p. 103324, 2024.

[47] Z. Xu, Y. Liu, G. Xu, and T. Lukasiewicz, "Self-supervised medical image segmentation using deep reinforced adaptive masking," *IEEE Transactions on Medical Imaging*, vol. Early Access, pp. 1–14, 2024.

[48] Z. Xu, W. Xu, R. Wang, J. Chen, C. Qi, and T. Lukasiewicz, "Hybrid reinforced medical report generation with m-linear attention and repetition penalty," *IEEE Transactions on Neural Networks and Learning Systems*, vol. Early Access, pp. 1–15, 2023.